Article:

Li, X, Jaworski, AJ and Mao, X orcid.org/0000-0002-9004-2081 (2018) Bubble size and bubble rise velocity estimation by means of electrical capacitance tomography within gas-solids fluidized beds. Measurement, 117. pp. 226-240. ISSN 0263-2241

https://doi.org/10.1016/j.measurement.2017.12.017

Bubble size and bubble rise velocity estimation by means of electrical capacitance tomography within gas-solids fluidized beds

Xiaoxu Li [1,3], Artur J. Jaworski [2,*], Xiaoan Mao [1]

[1] Faculty of Engineering, University of Leeds, Woodhouse Lane, Leeds LS2 9JT, United Kingdom
[2] School of Computing and Engineering, University of Huddersfield, Huddersfield HD1 3DH, United Kingdom
[3] Jiangsu Sunpower Technology Co. Ltd, No.2111, Chengxin Avenue, Science Park, Jiangning District, Nanjing, P.R. China, 211112

*Corresponding author: a.jaworski@hud.ac.uk

Abstract

Electrical capacitance tomography (ECT) has been developed as a non-invasive and non-intrusive measurement technique to investigate the internal hydrodynamic characteristics of gas-solids systems in fluidized beds. This paper describes an investigation, in which a customized twin-plane ECT sensor was designed and constructed to study the fluid flow processes within a bench-scale gas-solids fluidized bed. A detailed calibration process was conducted using hollow plastic balls of different diameters to derive the reference grey level cut-off values for determining the bubble diameter. In addition, numerical simulations were carried out to investigate the plastic ball wall effect on measured capacitance values. Bubble diameters were estimated by means of the individual reference cut-off values and their linear and second-order fitted curves. Linear back-projection (LBP) and iterative LBP image reconstruction algorithms were compared with respect to estimating the bubble diameter. A number of approaches were investigated to estimate the bubble rise velocity including three methods based on cross-correlation techniques and the detailed signal analysis. Bubble diameters were also obtained using a new approach based on "back-calculation" of the bubble rise velocity through widely accepted empirical correlations from the existing literature.

Keywords: Gas-solids fluidized beds, Electrical capacitance tomography, Bubble diameter, Bubble rise velocity, Numerical simulation

Nomenclature

Abbreviations/Acronyms

CMU	capacitance measurement unit
ECT	electrical capacitance tomography
Fps	frames per second
LBP	linear back-projection algorithm
LBP10	10-step iteration with linear back-projection algorithm

Latin symbols

A_t	the cross-sectional area of the bed
C_i	a new cut-off value obtained in the iteration loop
C_0	assumed step reduction of cut-off value
D	the bed diameter
D_B	the diameter of the sphere having the same volume as the bubble
D_{BM}	maximum possible bubble diameter
D_e	the equivalent ball diameter or bubble diameter
D_i	the initial bubble diameter
D_t	the tentative bubble diameter
d_0	initial bubble diameter
g	acceleration due to gravity
h	height in the bed
h_0	a constant characterizing the distributor
j	number of elementary steps of the time lag
k	row index for the location of pixels
K	the maximum value of row index for the location of pixels
l	column index for the location of pixels
L	the maximum value of column index for the location of pixels
N	number of samples in the discretised signal
n	element index of the signal sample
n_d	total number of orifices on the distributor plate
P	the time series of 32 x 32 pixel images for plane 1
Q	the time series of 32 x 32 pixel images for plane 2
$\hat{R}_{xy}$	cross-correlation function value

t_{b1}	time instant when a bubble appears at plane 1
t_{b2}	time instant when a bubble appears at plane 2
U	the superficial gas velocity
U_b	bubble rise velocity
U_{br}	single bubble rise velocity
U_{mf}	superficial gas velocity at incipient fluidization
$x(n)$	discretised ECT signal from plane 1
$y(n)$	discretised ECT signal from plane 2

Greek symbols

φ	constant parameter in Werther (1978) correlation for bubble rise velocity
$\nabla \cdot$	divergence operator
$\varepsilon(\boldsymbol{r})$	spatial permittivity distribution
$\varphi(\boldsymbol{r})$	electrical potential distribution
ε_{eff}	effective relative dielectric permittivity of the medium
ε_i	permittivity of the inclusions
ε_m	permittivity of the matrix
δ_i	volume fraction of the inclusions
ε_A	permittivity of the material A
ε_B	permittivity of the material B
$(\partial\varphi/\partial n)_A$	gradient of the electrical potential in the normal direction (from material A side)
$(\partial\varphi/\partial n)_B$	gradient of the electrical potential in the normal direction (from material B side)
δ	percentage error between D_t and D_i
δ_0	assumed percentage error
σ_N	the normalized two-dimensional cross-correlation coefficient
σ_{max}	the maximum value of two-dimensional cross-correlation coefficient
σ_{min}	the minimum value of two-dimensional cross-correlation coefficient
σ_{PQ}	the two-dimensional cross-correlation coefficient
Δx	the distance between the centres of the two measuring planes
Δt	elementary time step
Δt_i	the bubble time delay between plane 1 and 2

1. Introduction

Gas-solids fluidized beds have been playing a vital role in many industrial applications, such as chemical reactions, energy conversions, and physical contacting (Kunii and Levenspiel, 1991; Sasic et al., 2007; van Ommen et al., 2011). The reasons for their extensive utilization are twofold: the rapid and extensive solids mixing and high rates of heat and mass transfer between solid particles and gas phase (Geldart, 1986). Amongst different types of gas-solids fluidized beds, bubbling regime beds exhibit a high dynamic complexity and are attractive in a wide range of applications, especially in drying and food processing industry; it is believed that the variation of bubble properties contributes to their widespread usage (Makkawi and Wright, 2004).

Therefore, numerous researchers have studied the characteristics of the bubbling beds, especially in regard to bubble properties by means of several point-wise measurement techniques. Capacitance probes (Hage et al., 1996; Werther, 1999) were applied to derive bubble size (pierced length) and bubble frequency, and cross correlation techniques were utilized to detect the rise velocity of a single bubble with two separated probes (Werther and Molerus, 1973). Fibre optic probes were employed to not only determine local solid particle movements and the particle concentration (Oki et al., 1975) but also to characterize bubble features such as bubble size, bubble frequency, bubble rise velocity and bubble size distribution (Mainland and Welty, 1995; Rüdisüli et al., 2012). Pressure transducers inserted into the bed body were employed to determine the expanded bed height and bubble travelling time which was ultimately used to extract the bubble rise velocity (Chan et al., 1987; Werther, 1999).

Although useful conclusions have been drawn with respect to some fundamentals of gas-solids fluid flow processes, all the aforementioned point-wise measurement techniques are not able to effectively map the whole cross sectional area. In addition, they are intrusive in nature, which inevitably introduces disturbances to and interference with the internal fluid flow within the gas-solids fluidized beds (Li et al., 2016a; Rowe and Masson, 1981). Owing to the rapid developments in computing and instrumentation technology, tomographic measurement techniques – traditionally associated with medical imaging – have become a popular tool in multiphase flow measurements (Dyakowski et al., 2000). Among these, electrical capacitance tomography (ECT) has evolved into an inexpensive, non-intrusive, non-invasive, and easy to handle and operate measurement technique. Additionally, it poses no radiation hazard and can withstand a harsh industrial environment, including high pressure and high temperature (Yang, 2010).

2. Literature Review

ECT is a tomographic measurement technique which can give reconstructed images containing the information about concentration of one phase in a two-phase mixture by utilizing certain image reconstruction algorithms (Wang, 1998). During the past few decades, ECT has been developed and applied in many industrial applications, e.g. pneumatic and hydraulic conveying systems, bubbling columns and hydrocyclones (Dyakowski et al., 2000). More importantly, many previous researchers investigated important bubble characteristics including the bubble size and bubble rise velocity within gas-solids fluidized beds by capitalising on unique capabilities of ECT.

One of the earliest studies related to bubble sizes was conducted by the Morgantown Energy Technology Centre (Halow et al., 1993; Halow and Nicoletti, 1992) who observed bubble coalescence phenomenon in a 15.24 cm diameter fluidized bed using capacitance imaging system which contained 193 individual pixels. The frontal diameter of bubbles was estimated by assuming that they are hemispherical in shape, which was not always practically consistent with previous findings (Harrison et al., 1985). Due to the limited number of pixels, bubble boundary was not provided on a pixel basis, and only an average cross-sectional voidage (between 0.7 and 0.75) was utilized in deriving the bubble diameter. However, the obtained bubble diameter results were not compared with or validated against the existing empirical correlations. Wang (1998) and his co-workers (Wang et al., 1995) utilized an ECT system to investigate the flow pattern in the vicinity of an air distributor. The ECT system they used had 812 pixels distributed within the circular cross-section area of the 150 mm diameter bed vessel. Thus clearer boundaries between bubbles and emulsion phase were obtained; in addition, bubbling and slugging regimes were identified. It was concluded that bubble diameter for a bubbling fluidization was in the range of 0.5 - 1.5 cm. These values were compared with some empirical correlations, which indicated that the ECT system typically under-predicted the bubble diameter with an increase of the gas superficial velocity. Unfortunately, no deeper discussion was provided on the methods of estimating the bubble diameter, and in particular on identification of bubble boundaries which are normally defined based on a grey level “cut-off” value in a 32 by 32 pixel ECT image. Thus distinguishing between the gas bubble and emulsion phases was not clearly addressed.

In order to discover the influence of permittivity models on ECT image boundary sharpness (normally three models: parallel, in-series and Maxwell are available for a conventional ECT system), McKeen and Pugsley (2002) performed “phantom tests” using tubes made out of paper with 3.2 and 4.2 cm diameter. Linear back-projection (LBP) image reconstruction algorithm has been compared with iterative LBP reconstruction algorithm with the maximum number of iterations chosen as 500. Estimated equivalent tube diameters were compared with the expected values, which give different but relatively small errors for the various permittivity models tested. However, for the equivalent bubble diameter estimation within a gas-solids fluidized bed, they used directly the voidage contour of 0.7-0.8, indicated by Halow and his co-workers (Halow et al., 1993; Halow and Nicoletti, 1992) as the bubble boundary. However, no further discussion or reasoning was provided with respect to the determination process of the grey-level cut-off value. Moreover, a recent study by Chandrasekera et al. (2015) simply used three arbitrary bubble boundary values (0.4, 0.5 and 0.6) to estimate the bubble diameter within bubbling fluidized bed without giving any substantial clarification as to their choices. The obtained equivalent bubble diameter results were later compared with some widely accepted bubble diameter correlations. Therefore, it is fairly evident that a systematic investigation regarding the determination of the bubble boundary in ECT methods is required in order to characterize the bubble diameter in a reliable way.

Several researchers used cross-correlation techniques in order to determine the bubble rise velocity (Makkawi and Wright, 2002a; Wang, 1998). The basic idea is to identify the time lag between two series of ECT signals obtained from two ECT planes separated by a predefined distance (Yang and Liu, 2000). Some of the bubble rise velocity values obtained by means of cross-correlation techniques from ECT data were in good agreement with the predictions of empirical correlations (Makkawi and Wright, 2002a). Moreover, a "detailed signal analysis" method was proposed for the bubble rise velocity and the results were evaluated. However, all the bubble rise velocities were derived from the average solid fraction along the sensor volume. No experimental work has been conducted to address the effects of the pixel location on bubble rise velocity on a pixel-by-pixel basis within fluidized beds, although some preliminary attempts have been carried out for pneumatic conveying applications (Jaworski and Dyakowski, 2002).

Prior to further experimental work, it is useful to review several widely accepted empirical correlations for estimating bubble diameter and bubble rise velocity in order to facilitate the comparison and evaluation process. As for the bubble diameter, five popular correlations are chosen in this paper. They were chosen on the basis of an extensive review study by Karimipour and Pugsley (2011) which compared twenty-five correlations in total. Their details are summarized in **Table 1**. Far fewer correlations are available in the literature for calculating the bubble rise velocity. **Table 1** gives two of such empirical correlations which have been widely accepted by the research community.

Table 1 Empirical correlations for estimating bubble size and bubble rise velocity.

Category	Empirical correlation	Eqn. No.
Bubble size	$D_B = 0.54 \times (U - U_{mf})^{0.4} \times (h + 4{A_0}^{0.5})^{0.8}/g^{0.2}$ (Darton, 1977)	(1)
	$D_B = \left(U - U_{mf}\right)^{1/2}(h + h_0)^{3/4}\mathrm{g}^{1/4}$ (Rowe, 1976)	(2)
	$D_B = d_0[1 + 0.272 \times \left(U - U_{mf}\right)]^{1/3}(1 + 0.0684h)^{1.21}$ $d_0 = 0.853$ for Group B particles (Werther, 1978)	(3)
	$D_B = 0.38 \times h^{0.8}\left(U - U_{mf}\right)^{0.42} \times \exp[-0.25 \times \left(U - U_{mf}\right)^2 - 0.1\left(U - U_{mf}\right)]$ (Cai et al.,1994)	(4)
	$\frac{D_{BM} - D_B}{D_{BM} - d_0} = \exp(-0.3h/D)$ $d_0 = 0.347 \times \left\{A_t(U - U_{mf})/n_d\right\}^{2/5}$ $D_{BM} = 1.87d_0$ (Mori and Wen, 1975)	(5)
Bubble rise velocity	$U_b = U_{br} + \left(U - U_{mf}\right);\ U_{br} = 0.71 \times \sqrt{gD_B}$ (Davidson and Harrison, 1963)	(6)
	$U_b = \varphi\sqrt{gD_B}$ For Geldart B particles: $\varphi = \begin{cases} 0.64 & D \ll 10 \\ 0.254 \times D^{0.4} & 10 < D < 100 \\ 1.6 & D \gg 100 \end{cases}$ (Werther, 1978)	(7)

The overall aim of this paper is to investigate the bubble properties within bubbling regime in a bench-scale gas-solids fluidized bed by means of ECT measurements. The specific objectives are threefold: Firstly, to identify the most appropriate cut-off value in determining the bubble diameter within a 32 by 32 ECT image by virtue of a detailed calibration process using a range of plastic hollow balls. The effect of LBP and iterative LBP image reconstruction algorithms will be compared and evaluated. Secondly, to study the bubble rise velocity via a twin-plane ECT sensor whose two measuring electrode planes are separated by 40 mm. The bubble rise velocities estimated from cross-correlation analysis based on three different averaging approaches (presented in detail in section 4.3.2) will be evaluated against the ones obtained from the "detailed signal analysis" method and the empirical correlations. Finally, bubble diameters will also be obtained using two widely-accepted empirical correlations which contain the dependence between bubble size and bubble rise velocity (cf. **Table 1**). Here, the novelty lies in "back-calculating" the diameters from the known rise velocities.

3. Methodologies

The work described in this paper relies on both the experimental and numerical investigations. Therefore section 3.1 is devoted to the description of the bench-scale gas-solids fluidized bed set-up, ECT system and plastic ball calibration methodologies. Section 3.2 covers the numerical model built to investigate the effect of plastic ball on the capacitance values between measuring electrode pairs.

3.1. Experimental set-up

The experimental apparatus used in this study is presented in **Fig. 1**. Compressed air used for fluidization is provided from cylinder (1); the flow of air is controlled by a needle valve (2). Air flow rate is measured by a float type flow meter (3). The superficial gas velocity is obtained from the volume flow rate divided by the bed cross-sectional area. A piece of acrylic pipe (1 meter in length, internal diameter of 59 mm and wall thickness of 3 mm) forms the main body of the fluidized bed. In order to make the upward air flow as uniform as possible, a perforated PVC distributor (5) was designed and embedded between the bed pipe (7) and the air plenum (4). There are 48 holes of 1 mm diameter in total across the distributor cross section, which results in the total area of the holes of 3.768×10^{-5} m^2 (1.38% of the total effective area). To prevent any particles from falling down into the plenum, a piece of fine mesh was placed on top of the air distributor.

Silica sand with the density of 2650 kg/m^3 and the mean diameter of 276 microns was used as granular material, which belongs to the Geldard classification of Group B particles for fluidization (Geldart, 1973). **Figure 2** presents its size distribution and cumulative curves, which were obtained by Mastersizer2000 particle size distribution analyser. In order to keep the electrostatic field as two-dimensional as possible for the configuration calibration (Li et al., 2016b), the static height of the fluidized bed is kept at 170 mm so that the granular material can completely cover the ECT sensor electrodes (including guard electrodes). A customized cap (8) with an embedded fine mesh disk was mounted on top of the bed pipe to prevent the solids from blowing out of the bed.

Tomographic imaging was performed using a twin-plane ECT system (model PTL300E) made by Process Tomography Ltd. The capacitance measurement unit (CMU) (10) can measure inter-electrode capacitances in the range of 0.1 to 2000 fF and can provide the sampling rate of up to 200 frames per second (fps). The default PTL ECT32v2 software installed on the host PC (9) running Microsoft Windows XP is responsible for configuring the ECT system, recording inter-electrode capacitances, reconstructing images and displaying them at user-defined speeds (Process Tomography Ltd., 2001). ECT sensor (6) has 8 measuring electrodes per plane with the axial length of 10 mm. The centre-to-centre distance between two electrode planes (plane 1 is referred to as the lower plane) is 40 mm. Guard electrodes and external shielding electrodes are provided. A three dimensional drawing of the sensor geometry can be found in **Fig. 3(a)**.

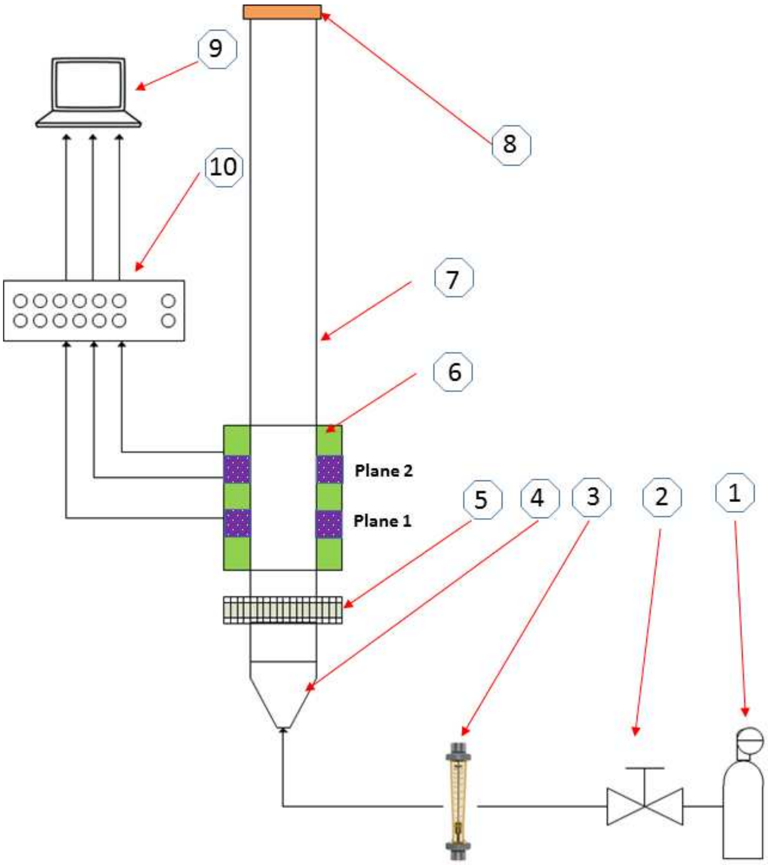

Fig. 1. Schematic diagram of experimental set-up. 1 – Compressed air cylinder; 2 – Needle valve; 3 – Float flowmeter; 4 – Plenum; 5 – Air distributor; 6 – Twin-plane ECT sensor; 7 – Fluidized bed vessel; 8 – Top-end cap; 9 – Host PC for ECT system; 10 – Capacitance measurement unit.

To fulfil the first objective of this paper, a series of hollow plastic balls (made of polypropylene) with different sizes were imaged to obtain the reference cut-off values. The main reason for choosing the spherical phantoms is that in a practical bubbling regime, the bubbles are more often of a three dimensional spherical shape (Rowe and Partridge, 1965, Li, 2016b). Use of two-dimensional phantoms (e.g. cylindrical objects used previously by others) would lead to an unphysical behaviour of electrical field and subsequent capacitance measurement (or incorrect numerical predictions in case of numerical work).

Information about the plastic balls used is summarized in **Table 2**. Clearly, the wall thickness is not identical for all ball sizes – this was because it was not possible to find a single manufacturer that would make a series of hollow ball sizes according to a consistent fabrication method. Ideally, the wall thickness should be as small as possible and of comparable dimensions for all five sizes, but this could not be achieved in the current study. To address this issue it has been decided to carry out a numerical investigation of the effects of wall thickness and permittivity combination on ECT inter-electrode capacitance measurements in order to estimate and eliminate any potential uncertainty in deriving the reference cut-off values caused by the inconsistent wall thicknesses. In order to traverse the phantoms in a settled bed, an M3 screw with a pierced head was tapped into the air distributor to act as an anchor for a fishing line. This goes through a plastic ball and is knotted on both sides to fix it onto the fishing line. The locations of the phantoms could be controlled (both vertically and radially) using different anchor points and phantom elevations; ECT measurements were then taken for calibration purposes.

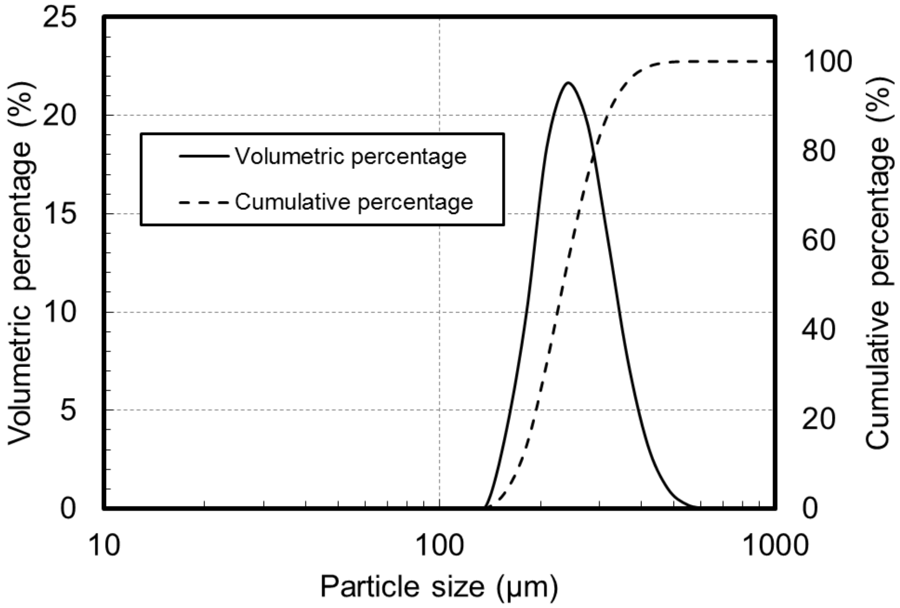

Fig. 2. Silica sand size distribution.

Table 2 Specifications of the five plastic balls.

No.	Outer diameter (mm)	Wall thickness (mm)	Internal diameter (mm)	Internal cross-sectional area (mm^2)	Mass (g)
1	10.0	1.20	7.60	45.34	0.275
2	18.4	1.60	15.20	181.36	1.355
3	20.0	0.84	18.32	263.46	0.920
4	25.4	1.30	22.80	408.07	2.250
5	40.0	0.38	39.24	1208.72	2.700

3.2. Numerical model description

The numerical simulation work was implemented using COMSOL Multiphysics software (version 5.2; Electrostatics Field AC/DC module). The electrical potential and the distribution of the relative dielectric permittivity are governed by Poisson's equation:

$$\nabla \cdot [\varepsilon(\boldsymbol{r})\nabla\varphi(\boldsymbol{r})] = 0\,, \tag{8}$$

where $\varepsilon(\boldsymbol{r})$ is the spatial permittivity distribution, $\nabla \cdot$ is the divergence operator and $\varphi(\boldsymbol{r})$ is the electrical potential distribution. The numerical simulation is three dimensional and the simulated capacitance results are derived from the surface integrals of the electrical charge density over the corresponding measuring electrode area, as explained by Dyakowski et al. (2000). **Figure 3(a)** presents the drawing of the model from COMSOL and **Fig. 3(b)** shows a section view of the three-dimensional model when a plastic ball is put inside the bed. The model was built within a cylindrical computational domain with the diameter five times the bed internal diameter. Zero charge condition was applied over the domain boundary. The excitation electrodes (two measurement electrodes in both planes and three guard electrodes) had electrical potential set at 1 volt. The remaining electrodes were set with electrical potential of zero volts. The computational domain was covered by 4,325,477 elements.

For the silica sand and air mixture forming the packed bed, an effective permittivity value was obtained from Maxwell-Garnett Equation (Dyakowski et al., 2000):

$$\left(\frac{\varepsilon_{\mathrm{eff}} - \varepsilon_{\mathrm{m}}}{\varepsilon_{\mathrm{eff}} + 2\varepsilon_{\mathrm{m}}}\right) = \delta_{\mathrm{i}}\left(\frac{\varepsilon_{\mathrm{i}} - \varepsilon_{\mathrm{m}}}{\varepsilon_{\mathrm{i}} + 2\varepsilon_{\mathrm{m}}}\right). \tag{9}$$

Here ε_{eff} is the effective relative dielectric permittivity of the medium (in this case, the mixture of the silica sand and air), ε_i is the permittivity of the inclusions; ε_m is the permittivity of the matrix; δ_i is the volume fraction of the inclusions. Clearly, equation (9) is derived for spherical inclusions, but it is widely used (e.g. Dyakowski et al., 2000) for mixtures of randomly shaped inclusions. In gas-solids mixtures, the settled/packed bed is also often assumed to have volume fraction of air equal to 0.4 (McCabe et al., 2001) which is also assumed here. It is also possible to treat equation (9) as "inclusions" of particles in the "matrix" of gas (the volumetric ratio of inclusions is 0.6), or alternatively as "inclusions" of gas in the "matrix" of solid material (the volumetric ratio of inclusions is 0.4). Both approaches were used for deriving the effective dielectric permittivity of the mixture (ε_{eff}=1.95 for air "matrix" and ε_{eff}=2.10 for solid "matrix") for further numerical simulations. In terms of other material properties, the measuring electrodes were set to copper. The permittivity value of the bed pipe was set to 2.7 (Acrylic), while the permittivity of the ball wall was set to either 2.2 (polypropylene), 2.10 (ε_{eff} for solid "matrix") or 1.95 (ε_{eff} for air "matrix") to observe the differences in the simulated capacitance values as discussed in Section 4.1. The ball dimensions used in the simulations were those summarised in **Table 2** for all five phantoms studied. The pipe dimensions were those given in the experimental setup description.

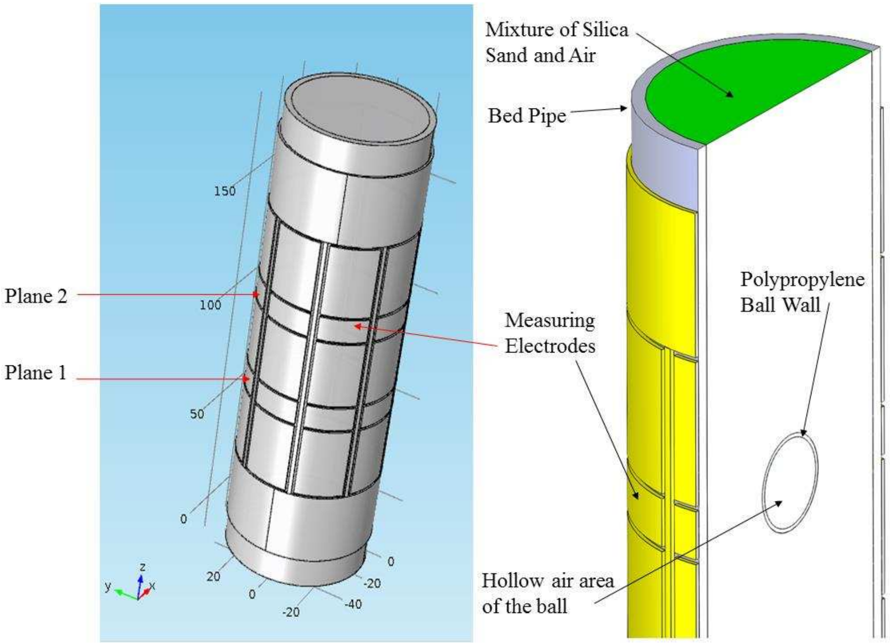

(a) **(b)**

Fig. 3. Schematic drawings: **(a)** three-dimensional model in COMSOL software; **(b)** section view of the model when a plastic ball is put inside the packed bed.

4. Results and discussion

The results of the numerical simulation will be addressed first in section 4.1 and then a detailed ECT calibration process using plastic balls will be introduced to derive the reference cut-off values from bubble images (section 4.2). Section 4.3 will cover the bubble rise velocity estimated using four approaches which include three cross-correlation methods based on different averaging approaches and the "detailed signal analysis" method. The final section 4.4 presents the results and discussion of the bubble size which is derived from the reference cut-off values and from "back-calculations" using the empirical equations for the bubble rise velocity.

4.1. Numerical simulation results

The numerical simulations have been executed for all five plastic balls and assuming four combinations of materials, referred to as "cases" later: (i) both bed and plastic ball wall permittivity 1.95; (ii) bed permittivity 1.95 and plastic ball wall permittivity 2.2; (iii) both bed and plastic ball wall permittivity 2.10 and (iv) bed permittivity 2.10 and plastic ball wall permittivity 2.2. Essentially, the aim was to check how well the inside of the plastic ball mimics an air bubble inside the bed. For brevity, only sample results for the 40 mm outer diameter ball, positioned at the pipe centre, are shown in **Fig. 4** and the capacitance data for all electrode pairs and four combinations of material are tabulated in Table 3. Clearly, due to the symmetry of the arrangement, only capacitance values for electrode pairs 1-2, 1-3, 1-4 and 1-5 need to be given.

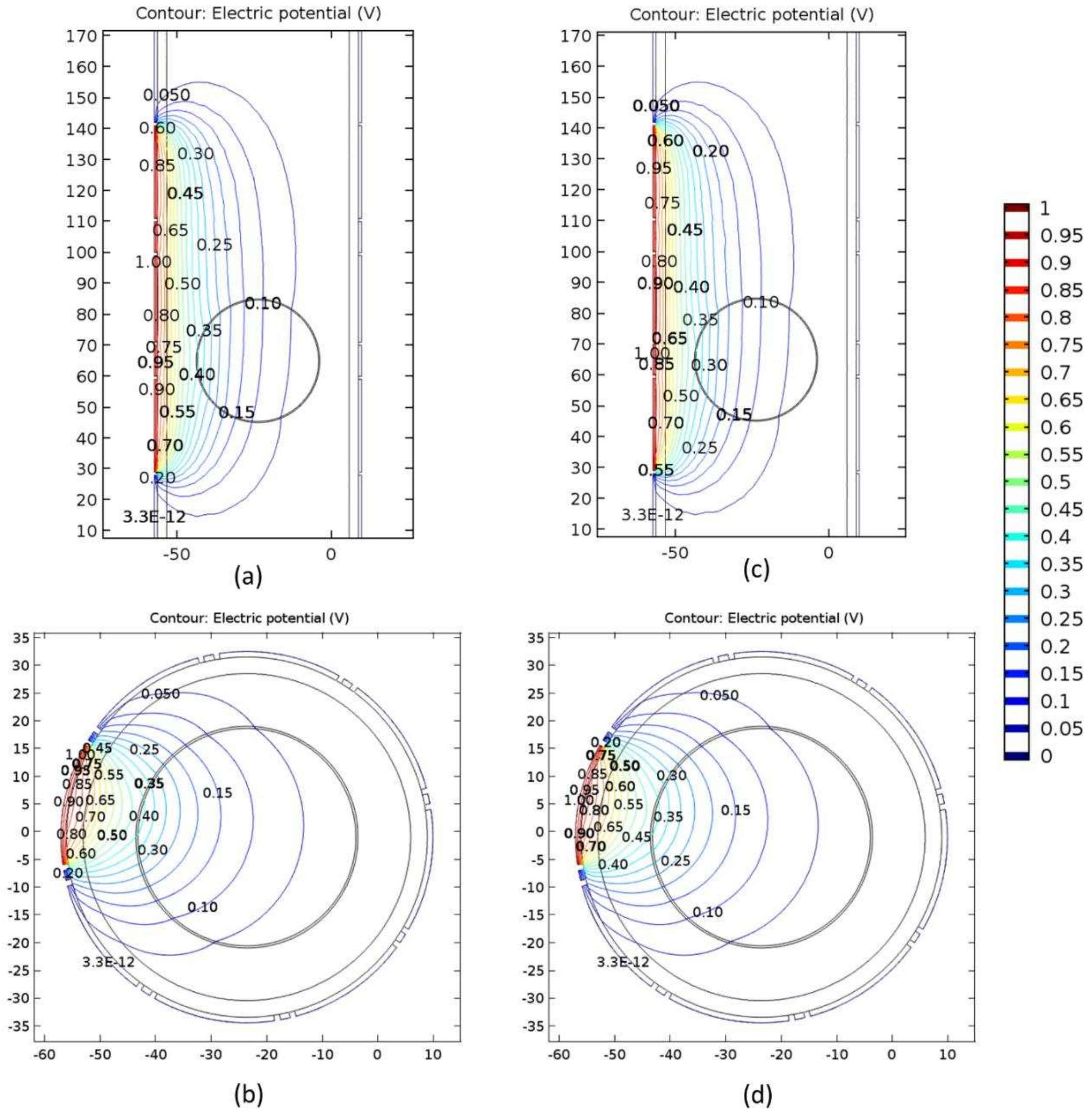

Fig. 4. Equipotential lines in longitudinal and transverse planes. **(a)** and **(b) -** case (i); **(c)** and **(d)** case (ii).

Figure 4 shows the equipotential line distributions in the longitudinal and transverse planes of the bed for a 40 mm ball placed in the centre of plane 1 of the ECT sensor. **Figures 4(a)** and **4(b)** concern case (i), while **Figs. 4(c)** and **4(d)** concern case (ii). It is worth noting that the equipotential lines bend on the boundaries between different dielectric materials (e.g. materials A and B) according to the "natural" boundary condition $\varepsilon_A(\partial\varphi/\partial n)_A = \varepsilon_B(\partial\varphi/\partial n)_B$, when the surface charge distribution on the interface between A and B is zero (direction n being perpendicular to the interface). However, it is hard to spot the differences between two electrical field distributions arising from a rather small change of the ball wall material permittivity from 1.95 to 2.2. Therefore, **Table 3** presents the inter-electrode capacitance values for pairs 1-2, 1-3, 1-4 and 1-5 to assist the quantitative study. The differences between capacitance values obtained for cases (i) and (ii) and between cases (iii) and (iv) indicate that the largest effect on the measured capacitance is around 0.03 fF which is below ECT system resolution. In terms of percentages the highest discrepancy appears for electrode pair 1-5 (0.357%). Similar analysis was carried out for the remaining ball sizes, giving the highest discrepancy of 0.676% (the discrepancy of inter-electrode capacitance for pair 1-5 being 0.04 fF for capacitance value of 6.36 fF). The numerical analysis suggests that the existence of the plastic ball wall would have a negligible effect on the ECT imaging of the "inside" of the ball that mimics the presence of an air bubble; and thus the reference cut-off value derivation process can be executed with confidence.

Table 3 Capacitance values for electrode pairs 1-2, 1-3, 1-4 and 1-5 obtained from numerical simulations and the percentage difference between two cases under each 'matrix' setting condition.

	When air is considered as 'matrix' (ε_{eff} = 1.95)		
Electrode pairs	Case (i): plastic ball wall permittivity: 1.95 (fF)	Case (ii): plastic ball wall permittivity: 2.2 (fF)	Percentage difference [%]
1-2	95.65	95.65	0.005
1-3	13.97	14.00	0.243
1-4	6.22	6.24	0.352
1-5	4.89	4.91	0.357
	When silica sand is considered as 'matrix' (ε_{eff}=2.10)		
Electrode pairs	Case (iii): plastic ball wall permittivity: 2.10 (fF)	Case (iv): plastic ball wall permittivity: 2.2 (fF)	Percentage difference [%]
1-2	97.80	97.80	0.002
1-3	14.76	14.77	0.095
1-4	6.51	6.52	0.133
1-5	5.09	5.10	0.135

4.2. Plastic ball calibration results

The position of the plastic ball "phantom" selected in this work included two cases, namely near the centre and near the wall of the bed. Each plastic ball was imaged at both locations at plane 2 level. In terms of image reconstruction, two algorithms were used for comparison: the linear back projection (LBP), regarded as the simplest method, and an iterative LBP algorithm (Yang et al., 1997) which has the capability to produce images of better quality, for example sharper boundaries between bubbles and the emulsion phase in the bubbling regime. The optimum number of iterations needs to be established by taking into account the sharpness of the resulting boundary and distortions of the reconstructed bubble shape (Li et al., 2016b). Based on such analysis, and comparisons with the basic LBP reconstruction, a 10-step iteration process was chosen as a trade-off and will be denoted as "LBP10" throughout. The parallel permittivity model in the ECT system was chosen since it has been regarded as the one having good accuracy based on phantom tests of McKeen and Pugsley (2002).

The main procedure for deriving reference cut-off values is summarized in **Fig. 5(a)**. Initially, a 32 x 32 pixel image is obtained when a plastic ball occupies the biggest area of the ECT sensor (Li et al., 2016b). The circular cross sectional area in the image has 812 effective pixels and is seen as the equivalent area of the fluidized bed pipe (ID 59 mm). The ratio of the plastic ball hollow area to the fluidized bed internal area is calculated, which allows calculating the corresponding pixel number equivalent to the hollow area of the ball. Then, the number of pixels in the image is counted starting from the lowest grey level until the cumulative number of pixels equals the pixel number occupied by the plastic ball. The largest value of these counted pixels is taken as the cut-off value for distinguishing the solid and air phases. This process is repeated for the five plastic balls at two locations under two image reconstruction algorithms. The derived reference cut-off values are summarized in **Table 4**. Note that the process of determining real bubble diameter using the obtained cut-off values is summarized in **Fig. 5(b)**, which will be addressed in more detail later in section **4.4**.

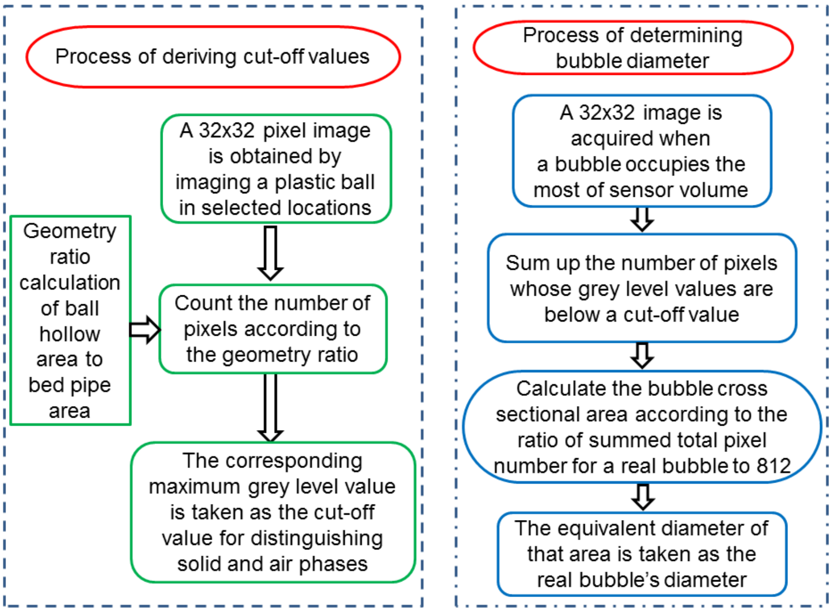

(a) **(b)**

Fig. 5. Flow charts for the process of: deriving the reference cut-off values **(a)** and determining bubble diameter **(b)**.

The effectiveness of the “cutting-off” process is illustrated in **Fig. 6** obtained for plastic ball No. 5 placed at the bed centre; image (a) is obtained using LBP10, while image (b) presents the processed image after applying the “cutting-off” process. It can be seen that qualitatively these two images give the same pattern of plastic ball No. 5. However, the second image has a sharper boundary simply because the pixels whose volume fraction value are less than the cut-off value (0.5383) are assigned the grey level value of 0 (black colour) whereas the ones whose volume fraction values are larger than the cut-off value are set to 1 (white colour). Symbol D_e shown in **Fig. 6(b)** denotes the equivalent ball diameter. In addition, during the process of deriving the cut-off value in this example the difference between the actual equivalent pixel number of the ball hollow area and the pixel number calculated using the derived cut-off value of 0.5383 (cf. **Table 4)** is only one pixel.

Table 4 Reference cut-off values derived for five plastic balls

No.	Outer diameter (mm)	Internal hollow diameter	Near centre		Near wall	
			LBP	Iteration 10	LBP	Iteration 10
1	10.0	7.60	0.9394	0.9000	0.9200	0.9000
2	18.4	15.20	0.7700	0.7540	0.6999	0.6700
3	20.0	18.32	0.7687	0.7700	0.6646	0.6400
4	25.4	22.80	0.6300	0.6482	0.4948	0.4600
5	40.0	39.24	0.5835	0.5383	0.4441	0.4293

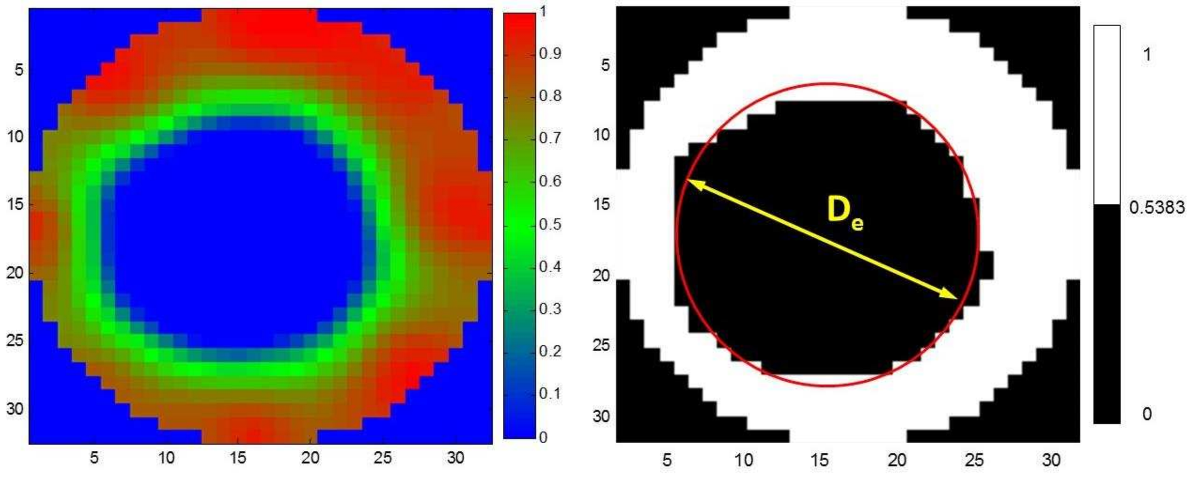

(a) **(b)**

Fig. 6. Images obtained when plastic ball No. 5 was placed near centre of the bed: before the cutting-off process **(a)** and after the cutting-off process **(b)**.

4.3. Bubble rise velocity

In the current study two methods were employed to derive the bubble rise velocity. The first one is based on cross-correlation techniques. Three formulations have been tried that differ in the type of averaging used to calculate the required time lag values, as is discussed in section 4.3.1. The second method uses the “detailed signal analysis” as described by Makkawi and Wright (2002b) which relies on identification of local minima of the averaged solid fraction signals at two measuring planes, corresponding to the passage of bubbles. The results obtained from both methods will be compared with two empirical equations given in **Table 1**.

4.3.1. Cross-correlation method

Broadly speaking the determination of the bubble rise velocity using cross-correlations relies on obtaining the time lag value between the signals recorded in two spatially separated locations (e.g. planes 1 and 2 in ECT system) and using a known separation distance. In the classic approach the two signals discretised in time: $x(n)$ and $y(n)$ where $n = 1, \dots, N$ are subject to correlation analysis (cf. Beck and Pląskowski, 1987):

$$\hat{R}_{xy}(j\Delta t) = \frac{1}{N}\sum_{n=1}^{N} x(n)y(n+j) \qquad j = 0,1,2,\dots,J. \tag{10}$$

Here, the correlation function value $\hat{R}_{xy}(j\Delta t)$ is calculated as a function of time lag $j\Delta t$ where Δt is an elementary time step arising from the sampling rate. The maximum of $\hat{R}_{xy}$ typically identifies the time lag taken for calculation of the propagation velocities of the flow structures of interest (e.g. bubble rise velocity). In the classic formulation the signals $x(n)$ and $y(n)$ are normalised values of the input signals obtained by subtracting a mean value and dividing by the value of the signal standard deviation, which ensures that the bounds of correlation function are ±1.

In the first cross-correlation approach tested in this study the input signals for the cross-correlation procedure are simply taken as cross-sectional average solids concentration in planes 1 and 2. **Figure 7** presents the normalized cross-correlation functions for different values of the superficial velocity. Clearly, finding the time lags corresponding to the maxima in the functions (generally between 0.7 and 0.8 in this example) allows calculation of propagation velocities using the know separation between planes of 40 mm.

The second cross-correlation approach uses the grey level values from individual pixels as input signals. In the ECT system used the bed cross section is divided into 812 pixels. The cross-correlation analysis is then conducted for the corresponding pixels in planes 1 and 2. Clearly, the normalized cross-correlation functions for each pixel pair will be similar to those plotted in **Fig. 7** and thus are omitted here. Subsequently a distribution of pixel-by-pixel propagation velocity values is obtained over the entire cross section as indicated in **Fig. 8**. In this approach a single value of the bubble rise velocity is obtained by averaging 812 velocity values obtained over the bed cross-section area.

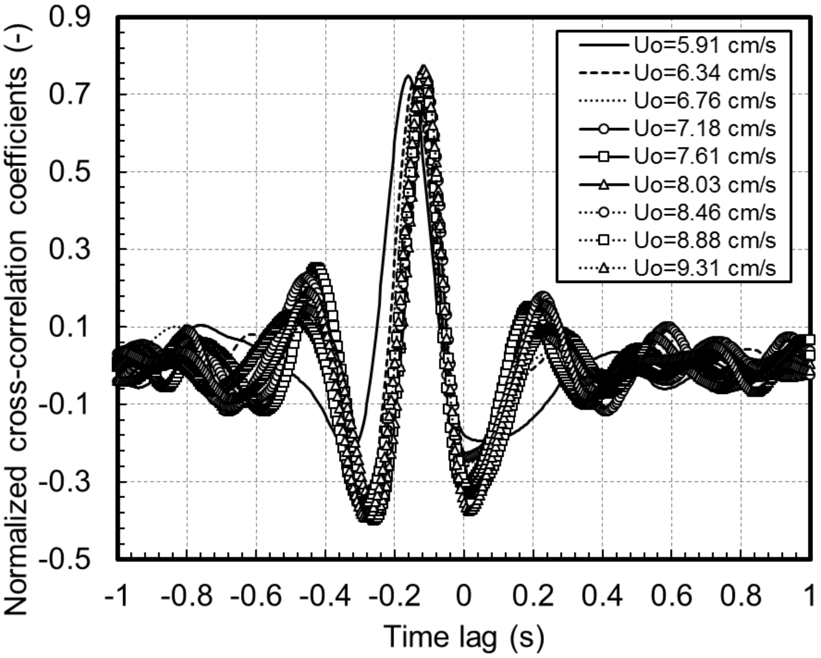

Fig.7. Normalized cross-correlation functions at various superficial gas velocities.

As it can be seen from **Fig. 8(a)**, when the gas superficial velocity is low at 5.91 cm/s, the bubble rise velocity is also low in a range of 20 to 35 cm/s for all the 812 pixels. It is also observed that the "surface" of the bubble rise velocity distribution is not uniform, which may well be attributed to certain preferred pathways of bubbles due to slight misalignments of the bed relative to the vertical direction or manufacturing errors in the distributor plate openings. Some more detail of the flow physics is also discussed by Li et al. (2017). When the gas superficial velocity increases (c.f. **Fig. 8(b) – (e)**), the maximum value of bubble rise velocity across the 812 pixels shows a slight increasing trend, i.e. the upper limit increases from 35 cm/s to 45 cm/s. This value drops to 40 cm/s with the further increase of the gas superficial velocity (shown in **Fig. 8(f)**), which can also be interpreted on the grounds of the bubble-slug transition as explained by Li et al. (2017).

Finally, the third cross-correlation method tested relies on applying the two-dimensional cross-correlation concept (Bourke, 1996). This is typically used for analysing photographic images, but can be easily adopted to ECT images (in essence 32 x 32 pixels in size) obtained from the two sensor planes. The mathematical expression for the calculation of such image-based cross-correlation function is conceptually similar to Equation (10), but differs in detail:

$$\sigma_{PQ}(j\Delta t) = \sum_{n=1}^{N}[\,\sum_{k=1}^{K}\sum_{l=1}^{L} P_{(n)}^{(k,l)}\, Q_{(n+j)}^{(k,l)}\,] \qquad (11)$$

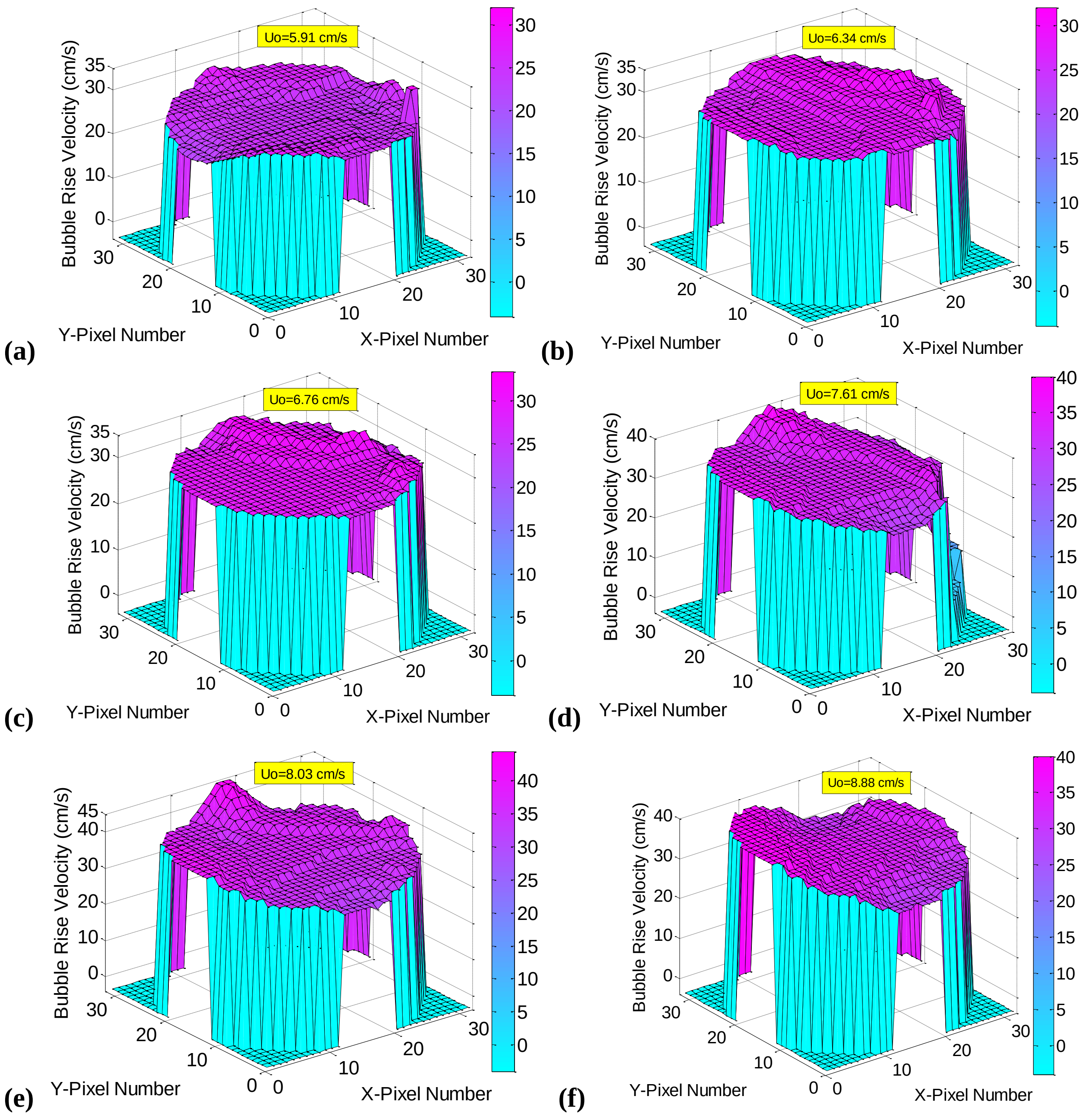

Fig. 8. Three dimensional distribution of propagation velocity obtained from pixel-by-pixel correlation analysis for superficial gas velocities: **(a)** 5.91 cm/s; **(b)** 6.34 cm/s; **(c)** 6.76 cm/s; **(d)** 7.61 cm/s ; **(e)** 8.03 cm/s; **(f)** 8.88 cm/s.

$$\sigma_N = \frac{\sigma_{PQ}(j\Delta t) - \sigma_{min}}{\sigma_{max} - \sigma_{min}} \tag{12}$$

Here, P and Q are the two time series of 32 x 32 pixel images for planes 1 and 2, respectively; k and l are the row and column index for the location of pixels ($k = 1, \dots, K$ and $l = 1, \dots, L$); K and L are the maximum pixel indices, both equal to 32 in this case; $n = 1, \dots, N$, where N is the number of samples in the cross-correlation calculation; Δt is an elementary time step arising from the sampling rate; j is the discrete counter of time lag ($j\Delta t$); $\sigma_{PQ}(j\Delta t)$ is the calculated image-based cross-correlation function; σ_N is the normalized cross-correlation coefficient. Clearly, the averaging performed here is on the level of products of P and Q inside the external summation over n. Execution with different time lags (in this case ± 1 s interval) is aided by a section of customized MATLAB codes. It should be noted that in the 32 x 32 pixel images, the corners (cf. **Fig. 6(a)**) are occupied by pixels outside the bed area – however these were allocated grey level values of zero and do not contribute mathematically to the calculated value of $\sigma_{PQ}(j\Delta t)$. The obtained normalized cross-correlation functions are displayed in **Fig. 9**.

It can be seen from **Fig. 9** that there are clear peaks in the 2D image-based cross-correlation function – similarly to **Fig. 7** the peaks occur for negative time lag values that is a consequence of adopted convention for labelling the ECT planes. It is worth noting that the maximum coefficient at the gas superficial velocity of 5.91 cm/s is at a time lag of zero, which is difficult to interpret (normally it would mean that the signal fluctuations are contemporaneous and thus propagation velocity infinite). However, because of the formulation of **Equation (11)** the "signals" fed into it cannot be normalized the same way as those fed into **Equation (10)** for the first two cross-correlation methods. However, for superficial gas velocities above the lowest value the realistic time lags can be established and propagation velocities calculated.

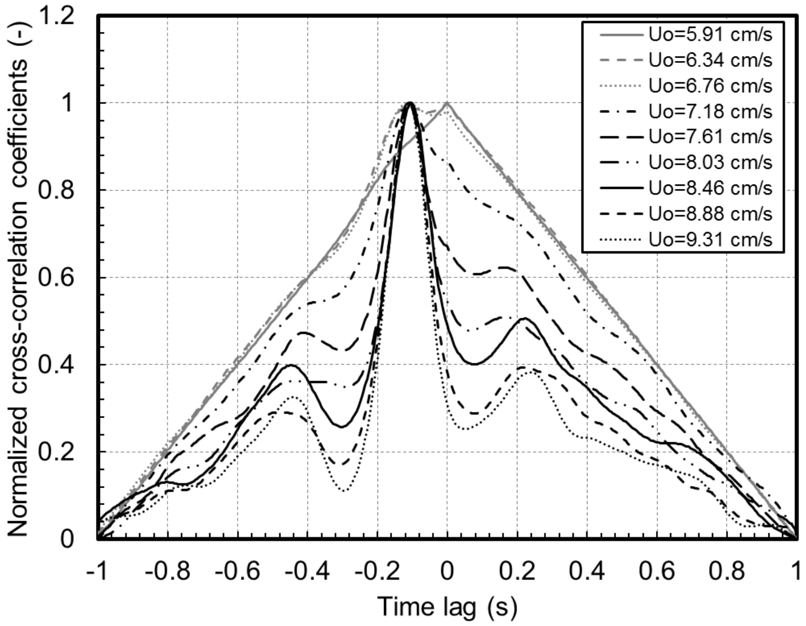

Fig. 9. Normalized cross-correlation functions for the 2D image-based correlation approach for different gas superficial velocities.

In order to evaluate the performance of the three cross-correlation approaches described above, the estimated bubble rise velocity together with the results obtained from two empirical correlations are presented in **Fig. 10**. It generally demonstrates that the bubble rise velocity estimated through first and second cross-correlation methods agree with each other and have broadly similar trends with both Davidson and Harrison and Werther equations – cf. **Equations (6)** and **(7)**. However Werther equation **(7)** also over-predicts the bubble rise velocity for very small superficial gas velocities and under-predicts for all other values of superficial gas velocities, while having a much "flatter" trend. Davidson and Harrison equation **(6)** seems to predict the bubble rise velocities correctly at both ends of the range of superficial gas velocities investigated and under-predicts slightly in the rest of the range – whilst having an overall trend seemingly more accurate than Werther equation **(7)**. In quantitative terms, the percentage error between results obtained using the first cross-correlation method and Davidson and Harrison equation **(6)** are all within 11.7% with the smallest values of 0.8% for the superficial gas velocity of 8.88 cm/s. Meanwhile, the largest percentage error between the first cross-correlation method and Werther equation **(7)** is around 18.4% at the superficial gas velocity of 8.02 cm/s. Overall the first cross-correlation method gives fairly good agreement with the two empirical correlations with the percentage error less than 20%. Very similar comments can be made about the comparisons between the second cross-correlation method and the two equations discussed. The application of the third cross-correlation method results in large discrepancies with the first and second method as well as the two empirical equations. The discrepancies are particularly large for the lower range of superficial gas velocities tested, but the accuracy also improves above the superficial gas velocity of 7.5 cm/s.

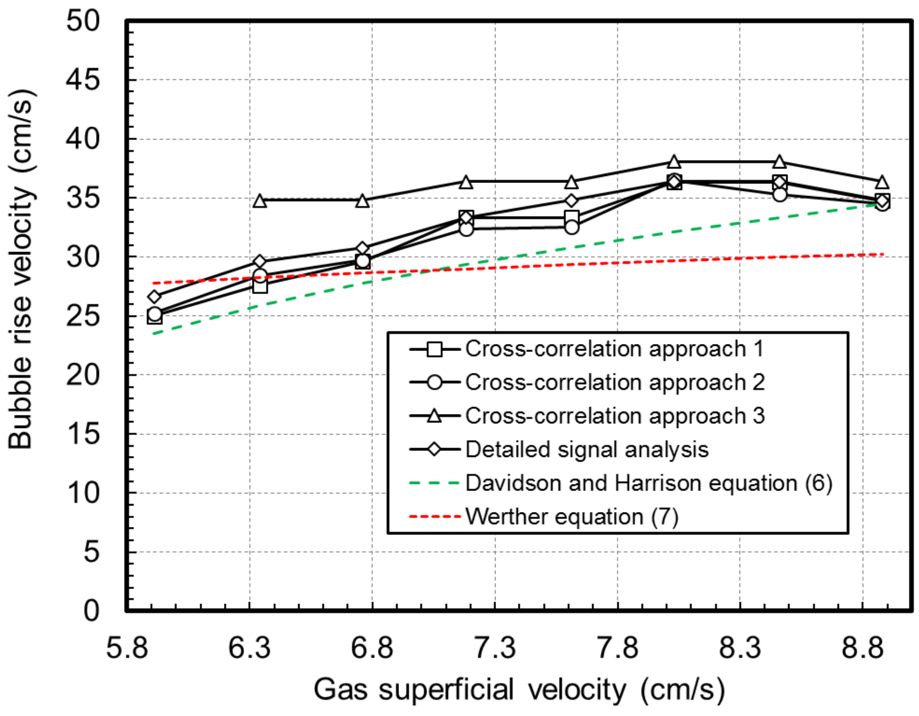

Fig. 10. Comparison of the estimated bubble rise velocity results between four different approaches and empirical correlation results at various gas superficial velocities.

4.3.2. Detailed signal analysis method

In addition to the cross-correlation methods, it is possible to extract the bubble rise velocity by analysing mathematically the averaged volume fraction data at both ECT measuring planes in a detailed manner (Makkawi and Wright, 2002b). Assuming a bubble appears at plane 1 at a time instant of t_{b1} and at plane 2 at a time instant t_{b2}, the time delay can be obtained in a straightforward manner by an appropriate MATLAB identification algorithm, and the rise velocity of a particular bubble can be calculated based on the separation distance between two measuring planes. The identification process of individual bubbles is repeated over the 80 s sampling time until an averaged bubble rise velocity is obtained. The mathematical method for determining bubble rise velocity is expressed as follows:

$$U_b = \frac{1}{N-1}\sum_{i=1}^{N}\frac{\Delta x}{\Delta t_i} \tag{13}$$

Where $\Delta t_i = t_{b2} - t_{b1}$ and Δx is the distance between the centres of the two measuring planes. The bubble rise velocities estimated using the detailed signal analysis method at various superficial gas velocities are also added to **Fig. 10**. The results broadly agree with the results obtained from the three different cross-correlation approaches and empirical correlations. However the agreement is much better with the results of the first and second cross-correlation method.

4.4. Bubble size

The bubble sizes are estimated in this work using two methods. The first one (described in section 4.4.1) utilizes the reference cut-off values presented in **Table 4** and the linear and second-order curves fitted around the data. LBP and LBP10 algorithms are also used and compared. The second method, discussed in section 4.4.2, relies on “back-calculating” the bubble sizes from the known bubble rise velocities using the two empirical equations for the bubble rise velocity presented in **Table 1**.

4.4.1. Bubble size obtained from reference cut-off values

A flow chart of the process of estimating the bubble diameter can be explained with reference to **Fig. 5(b)**. Suppose a 32 x 32 ECT image is acquired when a bubble occupies the most of sensor volume. The processing involves summing up the number of pixels whose grey level values are below a cut-off value (cf. **Table 4**). This is followed by calculating the bubble cross sectional area according to the ratio of the sum of the total pixel number for the imaged bubble to 812. The equivalent diameter (cf. **Fig. 6**) of that area is taken as the real diameter of the bubble. This process will be repeated for the whole experimental span of 80 s for each gas superficial velocity, and 20 times for the 20 cut-off values in the **Table 4**. The bubble diameters estimated by using the individual cut-off values with LBP and LBP10 algorithms are compared with the results estimated by the five widely used empirical correlations shown in **Table 1** (**equations (1)** – **(5)**). **Figure 11(a)** represents the results obtained with LBP algorithm using the cut-off values from phantoms placed near the centre, while **Fig. 11(b)** uses the cut-off values obtained using phantoms placed near the wall. **Figures 11(c)** and **(d)** represent analogous results based on LBP10 algorithm. All the bubble diameters are measured at the ECT plane 1 (the lower plane of the twin-plane sensor). The continuous lines in the graphs of **Fig. 11** represent the calculations of bubble diameters according to the empirical correlations for comparisons. The uncertainty in the bubble diameter was calculated by the standard deviation of the estimated bubble diameters under each superficial gas velocity.

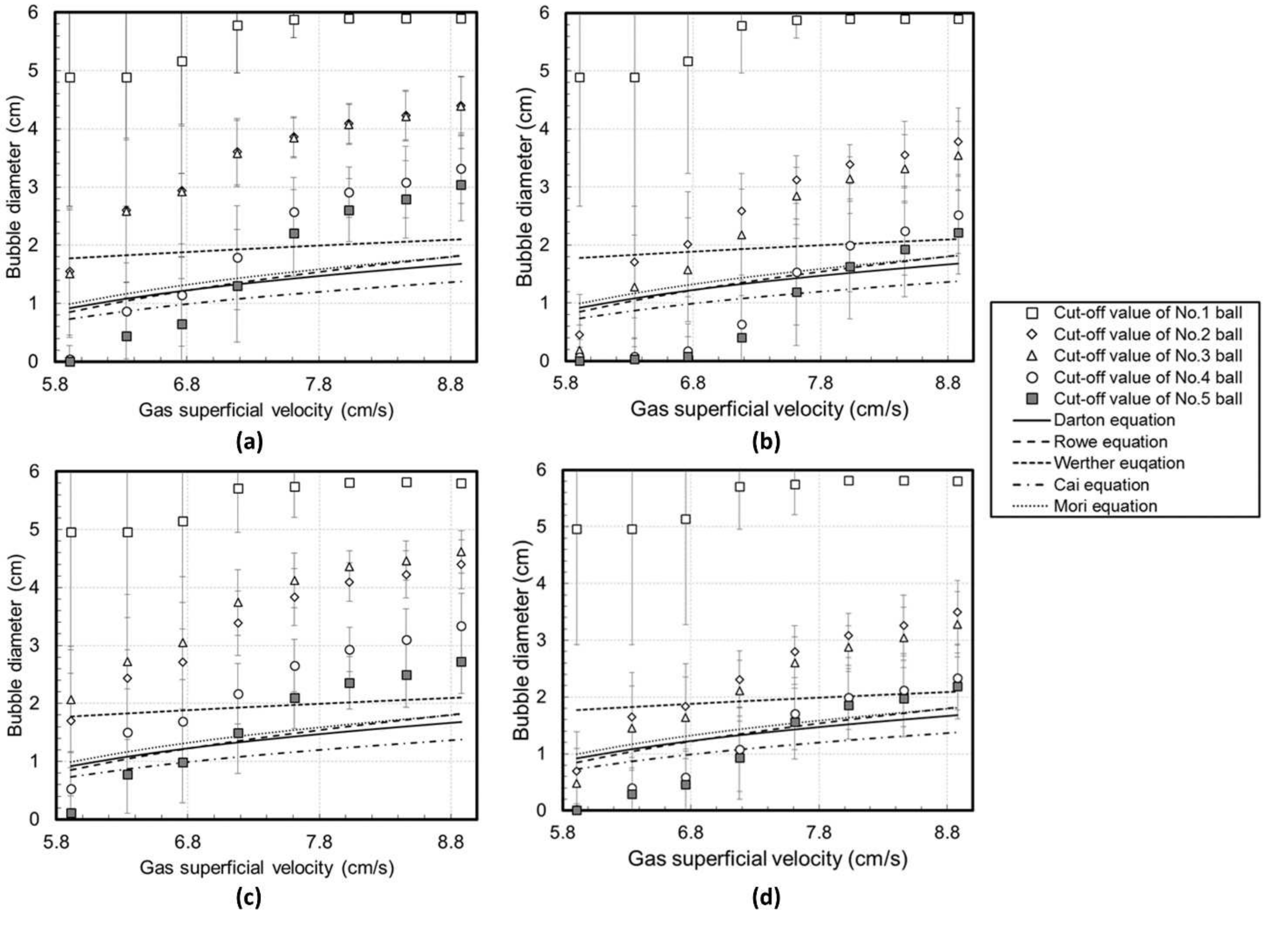

Fig. 11. Bubble diameter estimated with individual cut-off values using LBP algorithm: **(a)** near centre, **(b)** near wall, and using LBP10 algorithm: **(c)** near centre, **(d)** near wall.

In **Figs. 11(a)** and **(b)**, an apparent discrepancy can be identified between the bubble diameters obtained by using cut-off values derived from plastic ball No. 1 (for both near the centre and near the wall phantoms) and the bubble diameters estimated from five empirical correlations. This may be attributable to the fact that the internal diameter of the plastic ball No. 1 is about 7.6 mm, which is within the spatial resolution limits of ECT (normally 5% to 10% of the vessel diameter). Moreover, plastic ball No. 1 is so small that the cut-off values derived from it may not be valid since the size of the ball is probably not comparable with the size of real bubbles in a fluidized bed. In addition, the diameter is smaller than the axial length of the measurement electrodes. On the other hand, the results obtained with cut-off values from plastic balls No. 4 and 5 have a relative good consistency with the empirical correlation results, especially for higher gas superficial velocities. The results achieved with cut-off values from plastic balls No. 2 and 3 are very close to each other in **Fig. 11(a)**. However, it seems that better discriminated results are acquired in **Figs. 11(b)** – **(d)**. The reason behind this is not entirely clear, since there may be many additional contributing factors, for instance the ratio of the bubble to bed pipe diameter, the location of the bubble relative to the bed centre or the ratio between the bubble and electrode size etc. More research may be required in the future.

The results obtained in **Figs. 11(c)** and **(d)** demonstrate again that the estimated bubble diameters with cut-off values from the plastic ball No. 1 (for both near the centre and near the wall phantoms) have a pronounced discrepancy with the results from all the five empirical correlations. It indicates that the improved image reconstruction algorithm does not improve the size prediction in any significant way. However, it is interesting to find in **Fig. 11(c)** that the LBP10 algorithm helps to distinguish the bubble diameters estimated with the cut-off values from plastic balls No. 2 and 3, while the corresponding results “collapse” on each other in **Fig. 11(a)**. By comparing **Fig. 11(a)** with **(c)** and **Fig. 11(b)** with **(d)**, it can be seen that the agreement between experimental data and empirical equations is improved further for cut-off values obtained from plastic balls No. 4 and 5, especially for superficial gas velocities larger than 7.5 cm/s. A more detailed analysis of the results estimated with cut-off values from plastic ball No. 5 located near the centre reveals that there is an improvement in the percentage error from 26.2% (**Fig. 11(a)**) to 17.4% (**Fig. 11(c)**) when the superficial gas velocity is at 8.45 cm/s.

In order to further discover the effect of the reference cut-off values on the estimated bubble size in the bubbling regime, a linear curve fitting and a second-order curve fitting were implemented with respect of the derived reference cut-off values. It is plausible to assume that there are some defined relationships between the cut-off values themselves – postulated here as linear or second order. Then, the size of bubbles could be estimated via a linear or second-order curve fitting of the reference cut-off values. **Figure 12** shows such fitted curves with cut-off values obtained using phantoms near the centre and near the wall. **Figures 12 (a)** and **(b)** are for LBP algorithm and **Figs. 12(c)** and **(d)** are for LBP10 algorithm. It can be seen in **Fig. 12(a)** that the two linear fittings have a similar sloping trend when the cut-off values decrease with the increased internal hollow diameter. However, it appears that a better data fitting is achieved in **Fig. 12(b)** than **Fig. 12(a)**. To verify this hypothesis, one could examine the obtained bubble diameter results by using the corresponding fitted curves.

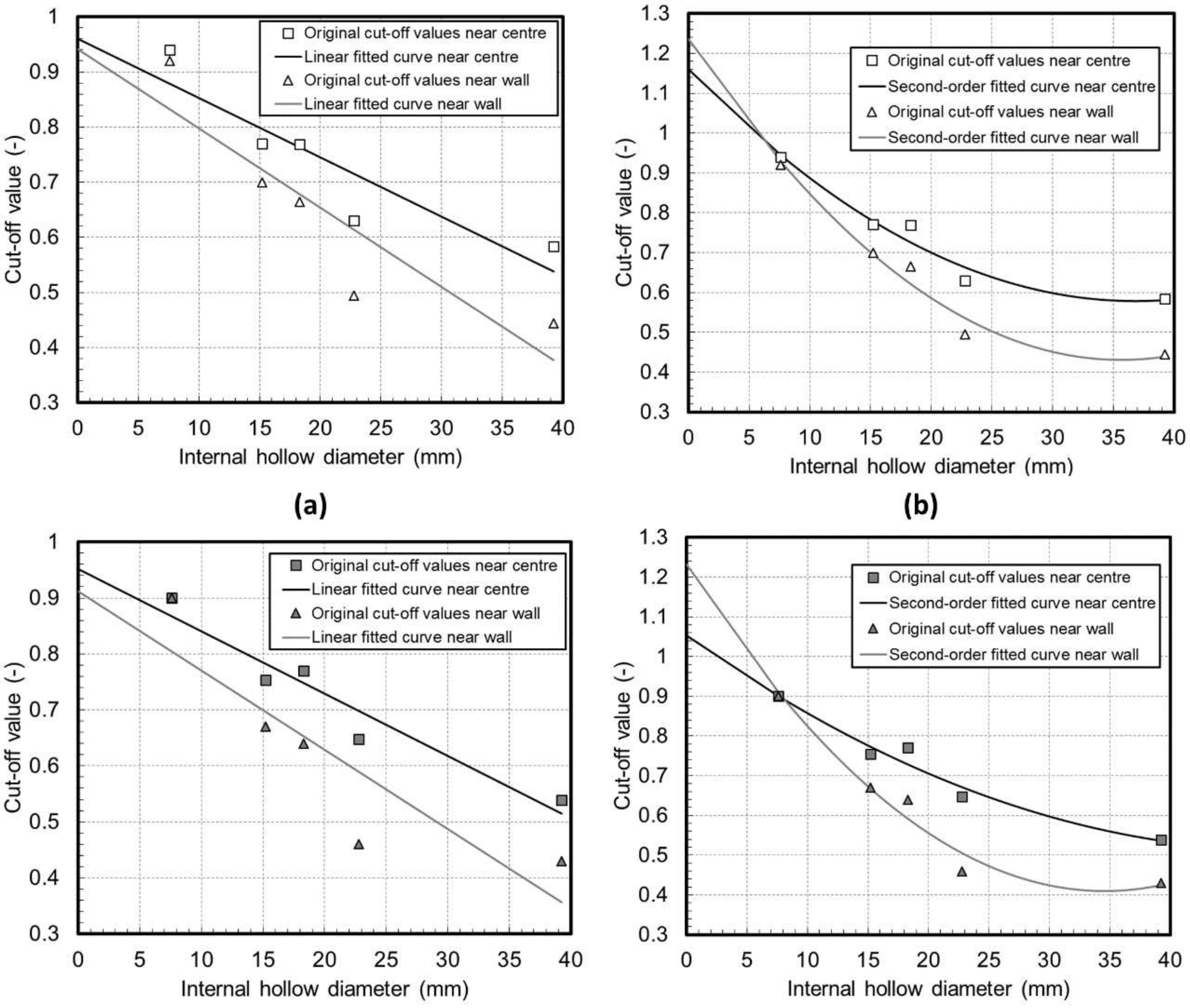

(a) (b)

(c) (d)

Fig. 12. (a) linear curve fitting for reference cut-off values using the LBP algorithm; **(b)** second-order curve fitting for reference cut-off values using LBP algorithm; **(c)** linear curve fitting for reference cut-off values using LBP10 algorithm; **(d)** second-order curve fitting for reference cut-off values using LBP10 algorithm.

The process of obtaining the bubble diameter by using the fitted curves can be described with reference to **Fig. 13**, showing an equivalent block diagram, as follows. Suppose one 32 x 32 ECT image is acquired at a time instant when the bubble occupies the most of the sensor volume. The process starts by assuming the bubble diameter is 1 mm (to ensure that any potential small bubbles are not missed). Then according to one specific fitted curve (there are eight curves in total in **Fig. 12**), there will be one corresponding cut-off value for that 1 mm bubble diameter. A tentative bubble diameter D_t can be temporally obtained by applying that cut-off value to the “flow sheet” given in

Fig. 5(b). Then, a comparison is made between the obtained D_t and the initial 1 mm bubble diameter D_i. If the percentage error δ between D_t and D_i is more than an assumed value δ_0, a new cut-off value will be chosen by a step reduction (by an assumed value C_0) from the previous cut-off value (cf. step "$C_i = C_i - C_0$"). After iterating the above process, a satisfactory equivalent bubble diameter will be acquired by evaluating the percentage error. The assumed percentage error and the step reduction are expected to be very small; in the present study they were chosen as $\delta_0 = 2\%$ and $C_0 = 0.0001$, respectively, taking into account the computational resources and convergence factors. Subsequently, the equivalent bubble diameter for a specific gas superficial velocity will be achieved by averaging all the calculated equivalent bubble diameter at different time instants for a time span of 80 second. It needs to be added that when the corresponding cut-off values are larger than 1 (as seen in **Figs. 12 (b)** and **(d)** due to second-order fitting), the procedure still works because the upper limit of the ECT grey level is in reality equal to unity regardless.

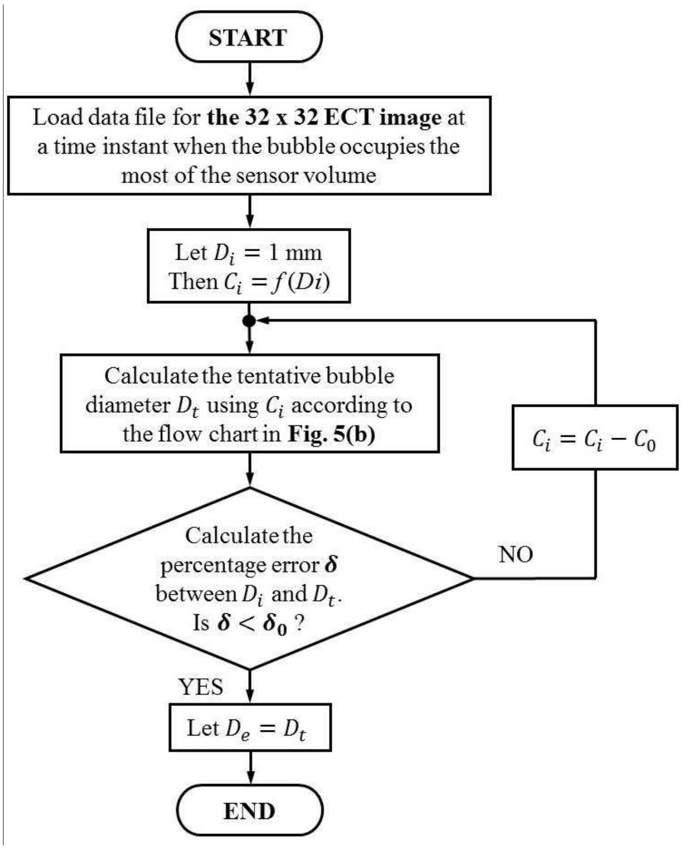

Fig. 13. Block diagram for estimating bubble diameter using reference cut-off values from fitted curves.

The bubble diameters obtained from the linear and second-order curve fitting (for both near the centre and near the wall phantom data) based on LBP algorithm (**Figs. 12(a)** and **(b)**) are shown in **Fig. 14**. In addition, the error bars in the figure were given as the standard deviation of the estimated bubble diameters. It can be seen that the estimated bubble diameters from Werther equation **(3)** give a generally good agreement with the results obtained from linear curve fitting of the cut-off values, especially when the gas superficial velocity is below 7 cm/s. The bubble diameters acquired with the linear curve fitting of the cut-off values near centre are larger than the ones obtained from the linear curve fitting of the cut-off values near wall. In terms of the second-order curves (near the centre cut-off values), they show a better agreement than using the linear curve fitting compared with Werther equation **(3)**. As for the results from the second-order curves (near the wall cut-off values), they also have a better agreement with the empirical results, i.e. compared with Mori and Wen equation **(5)**, than the results from the linear curves (near the wall cut-off values). All considered, the second-order curve fitting seems to give better results than the linear curve fittings across the studied range of superficial gas velocities. For brevity, the validation process will not be repeated here for the results using curve fitting presented in **Figs. 12(c)** and **(d)** since they lead to the same conclusions as **Figs. 12(a)** and **(b)**.

As demonstrated in **Fig. 14**, second-order curve fitting of the reference cut-off values is preferred. Therefore, to investigate the differences between LBP and LBP10 algorithms, only results using second-order fitting are shown in **Fig. 15**. It can be seen that the results obtained from the second-order fitting for near the centre phantom data using LBP10 have a better agreement with Werther equation **(3)** than the results obtained by using LBP when the superficial gas velocities are at 5.91 cm/s and 6.34 cm/s. The corresponding percentage errors are improved from 21.1% to 13.1% and from 6.3% to 0.4%, respectively.

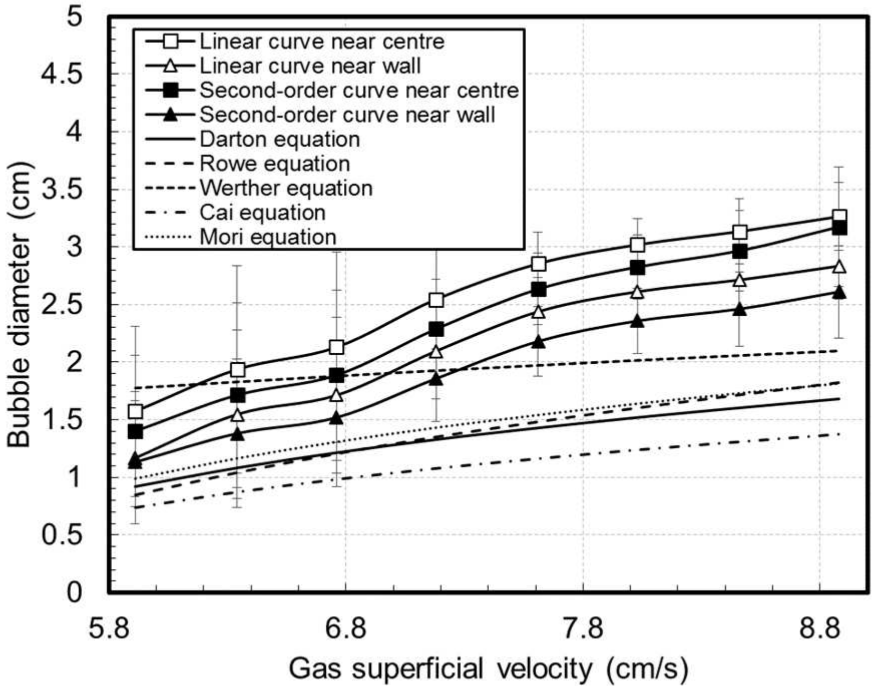

Fig. 14. Comparison between the bubble diameters derived from the linear and second-order fitting of reference cut-off values using LBP algorithm and empirical correlation results.

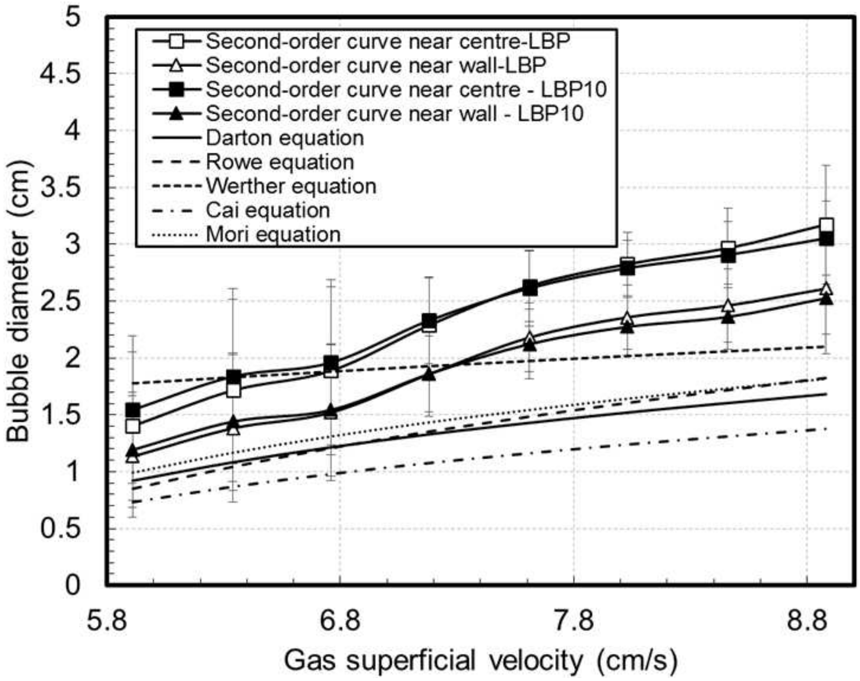

Fig. 15. Comparison between the bubble diameters derived from second-order fitting of reference cut-off values using LBP and LBP10 algorithms and empirical correlation results.

In addition, by comparing the results between the bubble diameters from the second-order curve (for near the wall cut-off values) using LBP10 and Werther equation **(3)** with the bubble diameters from the second-order curve (for near the wall cut-off values) using the LBP and Werther equation **(3)**, it can be observed that the averaged percentage difference has improved from 14.9% to 11%. Nonetheless, there are still some discrepancies between the results obtained by the various experimental methods – e.g. individual cut-off values and fitted curves (linear or second-order) of cut-off values – and the results estimated from empirical correlations. This may stem from the fact that there are probably some unforeseen limitations in using empirical correlations since the experimental set-up and conditions used in the present study inevitably differ from the ones utilized by previous investigators who proposed the empirical correlations. However, the reference cut-off values derived from the plastic ball calibration have been shown to be effective in estimating the bubble diameter in the bubbling regime of the gas-solids fluidized bed.

4.4.2. Bubble size obtained from bubble rise velocity results

As can be seen from **Table 1**, two empirical equations – **(6)** and **(7)** – contain the dependence between the bubble diameter and bubble rise velocity. Therefore, it is possible to "back-calculate" the bubble diameter using the known bubble rise velocity results obtained in section 4.3. For completeness, all four sets of bubble rise velocity results (cf. **Fig. 10**) will be used as the input bubble rise velocity data.

The back-calculated bubble diameters are presented in **Fig. 16** which also provides a comparison with the results obtained from the five empirical equations from the top of **Table 1**. To simplify the legend, results obtained from the five empirical correlations for bubble size estimation will be denoted according to their sequential number, i.e. "Eq.1" for Darton equation. Results obtained from cross-correlation approaches denoted as "first", "second" and "third" in section 4.3.1 will be denoted as "Xcorr 1", "Xcorr 2" and "Xcorr 3", respectively (with addition of the relevant equation number from **Table 1**, e.g. "–Eq.6" or "–Eq.7").

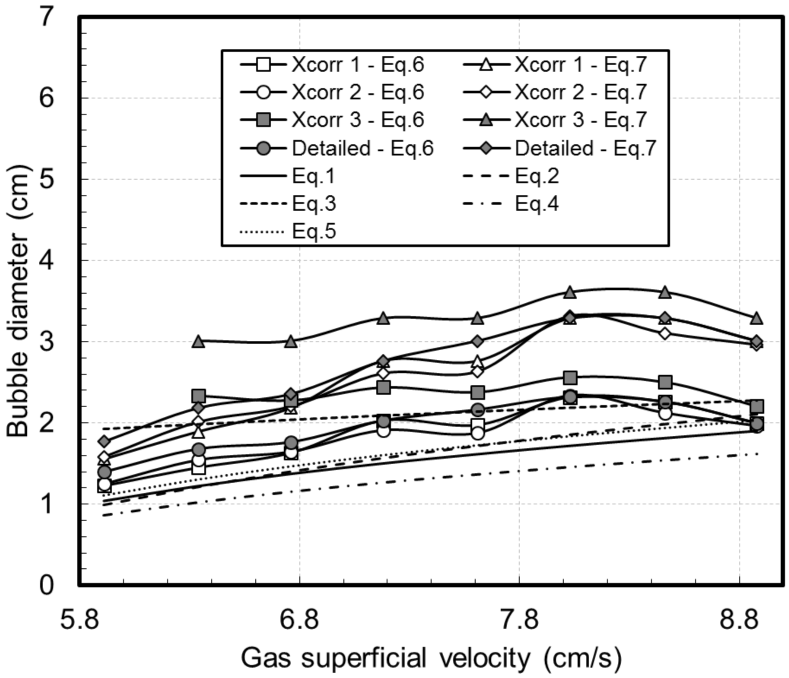

Fig. 16. Comparison between the back-calculated bubble diameter and the results from the five bubble diameter empirical equations.

It is worth noting that all the bubble rise velocities used here are the average values between two measuring planes. Hence, it is necessary to choose an average measuring plane height (averaged height of planes 1 and 2) when deciding the parameter of h for the five empirical correlations in **Table 1**. Therefore, the bubble size results obtained from the five empirical correlations shown in **Fig. 16** are slightly higher than the results shown in previous figures such as **Fig. 15**, whose relevant parameter of h would be the height up to the centre point of plane 1. **Figure 16** clearly shows that the back-calculated bubble diameter results broadly show a similar trend with the five empirical equations. In particular, the results from the first and second cross-correlation methods combined with Davidson and Harrison equation **(6)** demonstrate the best fit, whilst appearing between Werther **(3)** and Mori and Wen **(5)** equation plots. However, the results from the third cross-correlation method combined with either Werther equation **(7)** or Davidson and Harrison equation **(6)** show large deviations from the bubble sizes obtained from empirical equations. This is the reflection of the original slight deviation in the bubble rise velocity using the third cross-correlation as shown in **Fig. 10**. Overall, the back-calculated bubble diameter from the bubble rise velocity shows a good agreement with the five empirical equations. Furthermore, it re-confirms the effectiveness of deriving bubble rise velocity by means of the cross-correlation techniques. More importantly, it has been shown that the bubble size can be "back-calculated" from bubble rise velocity with sufficient confidence.

5. Conclusions

Bubble characteristics have been investigated by means of a customized twin-plane ECT sensor using a bench-scale gas-solids fluidized bed. In terms of bubble size estimation, a detailed calibration process using five different sizes of spherical phantoms was carried out to derive the reference cut-off values for estimating bubble diameter. This was combined with numerical simulations to evaluate the phantom wall effects on the measured capacitance values. Individual reference cut-off values and their linear and second-order fitting have been studied for deriving bubble diameter compared to five empirical equations available in the literature. Bubble diameters obtained from the individual cut-off values suggest that the cut-off values from phantom No. 1 were not suitable for a reasonable bubble diameter estimation. Instead, the cut-off values obtained from phantoms No. 4 and 5 result in a better agreement between the estimated bubble diameter and the results calculated from the five empirical equations. In general, results estimated from the second-order curve fitting showed a better data agreement than linear curve fitting, compared with the five empirical equations. The estimated bubble diameter using cut-off values from phantoms placed near the wall show a better performance than the cut-off values from phantoms placed near the centre.

The bubble rise velocity were estimated by means of four different approaches (including three different cross-correlation methods and the detailed signal analysis method). By comparing the results with two widely used empirical correlations, the cross-correlation approaches based on cross-sectional averaged solids concentration (first method) and averaged velocity distribution from the pixel-by-pixel approach (second method) are shown to be effective in deriving bubble rise velocity. In addition, bubble diameter results obtained by the new approach of "back-calculation" from four sets of bubble rise velocity results using equations **(6)** and **(7)** showed a fairly good agreement with the five empirical equations (given as **(1)** through to **(5)**) for bubble diameter, which demonstrates the potential of predicting bubble size using bubble rise velocity results.

Acknowledgements

The first author would like to acknowledge the maintenance funding from The China Scholarship Council (CSC) (Ref: 201206710052) and tuition fees funding from the School of Civil Engineering, University of Leeds in support of his PhD programme. Mr Robert Harris, Mr David Instrell and Mr Gurdev Bhogal are gratefully acknowledged for their help in setting up the experimental apparatus. The authors would also like to thank Professor Mi Wang from the University of Leeds and Professor Will Zimmerman from the University of Sheffield for useful discussions regarding some of the methods used in this research. Finally, the authors would like to acknowledge the consecutive loans of PTL300E systems from Professor Mi Wang, colleagues form EEE, University of Manchester and PTL, Cheshire, which enabled an uninterrupted progress of the first author's PhD programme.

References

BECK, M. S. & PLĄSKOWSKI, A. 1987. Cross correlation flowmeters, their design and application, CRC Press.

CAI, P., SCHIAVETTI, M., DE MICHELE, G., GRAZZINI, G. & MICCIO, M. 1994. Quantitative estimation of bubble size in PFBC. Powder technology, 80, 99-109.

CHAN, I., SISHTLA, C. & KNOWLTON, T. 1987. The effect of pressure on bubble parameters in gas-fluidized beds. Powder Technology, 53, 217-235.

CHANDRASEKERA, T., LI, Y., MOODY, D., SCHNELLMANN, M., DENNIS, J. & HOLLAND, D. 2015. Measurement of bubble sizes in fluidised beds using electrical capacitance tomography. Chemical Engineering Science, 126, 679-687.

DARTON, R. 1977. Bubble growth due to coalescence in fluidized beds. Chem. Eng. Res. Des., 55, 274-280.

DAVIDSON, J. F. & HARRISON, D. 1963. Fluidised particles, Cambridge University Press London.

DYAKOWSKI, T., JEANMEURE, L. F. & JAWORSKI, A. J. 2000. Applications of electrical tomography for gas–solids and liquid–solids flows—a review. Powder technology, 112, 174-192.

GELDART, D. 1973. Types of gas fluidization. Powder technology, 7, 285-292.

GELDART, D. 1986. Gas fluidization technology.

HAGE, B., WERTHER, J., NARUKAWA, K. & MORI, S. 1996. Capacitance probe measurement technique for local particle volume concentration in circulating fluidized bed combustors. Journal of chemical engineering of Japan, 29, 594-602.

HALOW, J., FASCHING, G., NICOLETTI, P. & SPENIK, J. 1993. Observations of a fluidized bed using capacitance imaging. Chemical Engineering Science, 48, 643-659.

HALOW, J. & NICOLETTI, P. 1992. Observations of fluidized bed coalescence using capacitance imaging. Powder Technology, 69, 255-277.

HARRISON, D., CLIFT, R. & DAVIDSON, J. F. 1985. Fluidization, Academic Press.

JAWORSKI, A. J. & DYAKOWSKI, T. 2002. Investigations of flow instabilities within the dense pneumatic conveying system. Powder Technology, 125, 279-291.

KARIMIPOUR, S. & PUGSLEY, T. 2011. A critical evaluation of literature correlations for predicting bubble size and velocity in gas–solid fluidized beds. Powder Technology, 205, 1-14.

KUNII, D. & LEVENSPIEL, O. 1991. Fluidization engineering, Butterworth-Heinemann Boston.

LI, X., JAWORSKI, A. & MAO, X. 2016a Application of a Twin-plane Electrical Capacitance Tomography Sensor for Characterising Bubble Behaviour in a Gas-solids Fluidized Bed. Proceedings of World Congress on Engineering 2016, London, UK. 29 June - 1 July.

LI, X., JAWORSKI, A. & MAO, X. 2016b. Investigation of bubble behaviour in a gas-solid fluidized bed by means of a twin-plane ECT sensor. 8th World Congress on Industrial Process Tomography, Iguassu Falls, Brazil.

Li, X., JAWORSKI, A. & MAO, X. 2017. Comparative study of two non-intrusive measurement methods for bubbling gas-solids fluidized beds: electrical capacitance tomography and pressure fluctuations. Flow Measurement and Instrumentation (in press, doi: 10.1016/j.flowmeasinst.2017.08.002).

MAINLAND, M. E. & WELTY, J. R. 1995. Use of optical probes to characterize bubble behavior in gas‐solid fluidized beds. AIChE Journal, 41, 223-228.

MAKKAWI, Y. & WRIGHT, P. 2002a. Fluidization regimes in a conventional fluidized bed characterized by means of electrical capacitance tomography. Chemical Engineering Science, 57, 2411-2437.

MAKKAWI, Y. & WRIGHT, P. 2002b. Optimization of experiment span and data acquisition rate for reliable electrical capacitance tomography measurement in fluidization studies—a case study. Measurement Science and Technology, 13, 1831.

MAKKAWI, Y. T. & WRIGHT, P. C. 2004. Electrical capacitance tomography for conventional fluidized bed measurements—remarks on the measuring technique. Powder technology, 148, 142-157.

McCabe, W.E., Smith, J.C., & Harriott,P. 2001. Unit operations of chemical engineering, McGraw Hill, New York.

MCKEEN, T. R. & PUGSLEY, T. S. 2002. The influence of permittivity models on phantom images obtained from electrical capacitance tomography. Measurement Science and technology, 13, 1822.

MORI, S. & WEN, C. 1975. Estimation of bubble diameter in gaseous fluidized beds. AIChE Journal, 21, 109-115.

OKI, K., AKEHATA, T. & SHIRAI, T. 1975. A new method for evaluating the size of moving particles with a fiber optic probe. Powder Technology, 11, 51-57.

Bourke, P., 1996. Cross correlation. Cross Correlation, Auto Correlation—2D Pattern Identification.

PROCESS TOMOGRAPHY LTD 2001. ECT User Guide. PTL300E Application Note

ROWE, P. & MASSON, H. 1981. Interaction of bubbles with probes in gas fluidised beds. Transactions of the Institution of Chemical Engineers, 59, 177-185.

ROWE, P. N. 1976. Prediction of bubble size in a gas fluidised bed. Chemical Engineering Science, 31, 285-288.

RÜDISÜLI, M., SCHILDHAUER, T. J., BIOLLAZ, S. M. & VAN OMMEN, J. R. 2012. Bubble characterization in a fluidized bed by means of optical probes. International Journal of Multiphase Flow, 41, 56-67.

SASIC, S., LECKNER, B. & JOHNSSON, F. 2007. Characterization of fluid dynamics of fluidized beds by analysis of pressure fluctuations. Progress in energy and combustion science, 33, 453-496.

VAN OMMEN, J. R., SASIC, S., VAN DER SCHAAF, J., GHEORGHIU, S., JOHNSSON, F. & COPPENS, M.-O. 2011. Time-series analysis of pressure fluctuations in gas–solid fluidized beds–A review. International Journal of Multiphase Flow, 37, 403-428.

WANG, S. 1998. Measurement of fluidization dynamics in fluidized beds using capacitance tomography. PhD Thesis.

WANG, S., DYAKOWSKI, T., XIE, C., WILLIAMS, R. & BECK, M. 1995. Real time capacitance imaging of bubble formation at the distributor of a fluidized bed. The Chemical Engineering Journal 56**,** 95-100.

WERTHER, J. 1978. Effect of gas distributor on the hydrodynamics of gas fluidized beds. German Chemical Engineering, 1**,** 166-174.

WERTHER, J. 1999. Measurement techniques in fluidized beds. Powder Technology, 102**,** 15-36.

WERTHER, J. T. & MOLERUS, O. 1973. The local structure of gas fluidized beds—I. A statistically based measuring system. International Journal of Multiphase Flow, 1**,** 103-122.

YANG, W. 2010. Design of electrical capacitance tomography sensors. Measurement Science and Technology, 21**,** 042001.

YANG, W., GAMIO, J. & BECK, M. 1997. A fast iterative image reconstruction algorithm for capacitance tomography. Sensors and their Applications, 8**,** 47-52.

YANG, W. & LIU, S. 2000. Role of tomography in gas/solids flow measurement. Flow measurement and Instrumentation, 11**,** 237-244.